Petroleum Research 11 (2026) 880–894

Contents lists available at ScienceDirect

Petroleum Research

journal homepage: http://www.keaipublishing.com/en/journals/petroleum-research/

Influence of fracturing fluid rheology on proppant transport and elbow erosion: A comparative CFD-DEM study

Chun-Rong Wang [a], Peng Wang [a,b], Xing-Yang Guo [a], Shi-Wei Qiao [a], Jian-Ping Yuan [a], Yan-Dong Gu [c], Fan Meng [d], Qiao-Rui Si [a,*]

[a] Research Center of Fluid Machinery Engineering and Technology, Jiangsu University, Zhenjiang, 212013, China
[b] Shandong Shuanglun Co.,Ltd. Weihai Shangdong 264209, China
[c] Yangzhou Univ, Coll Hydraul Sci & Engn, Yangzhou 225009, China
[d] School of Mechanical Engineering, Changzhou Institute of Technology, Changzhou 213032, China

ARTICLE INFO

Article history:
Received 5 August 2025
Received in revised form
6 December 2025
Accepted 12 January 2026
Available online 14 January 2026

Keywords:
Hydraulic fracturing
Erosion
Proppant transport
CFD-DEM
Shear-thinning fluid
Two-phase flow
Elbow pipe

ABSTRACT

To enable the precise prediction and control of erosion in hydraulic fracturing pipelines, this study employs a CFD-DEM method coupled with a wear model to quantitatively analyze the influence of shear-thinning fracturing fluids on proppant transport and elbow erosion. The study reveals a critical, non-monotonic effect of fluid concentration on erosion. Compared to the water baseline, the low-concentration (0.2%) fluid, by enhancing particle impact kinetic energy, counter-intuitively caused the maximum elbow erosion rate to surge by approximately 40%. However, as the concentration was further increased to 0.4%, the fluid's effective viscosity became dominant, causing the maximum erosion rate to plummet relative to the 0.2% case, ultimately falling to a level ~8% below the water baseline. More importantly, the high-concentration fluid altered particle trajectories, leading to a significant shift of the peak erosion zone from the elbow's midpoint (~77°) to its outlet (90°). This finding quantifies the complex impact of fracturing fluid rheology on erosion and provides critical data and a new perspective for proactively managing pipeline integrity by optimizing the fluid's non-Newtonian properties.

© 2026 Chinese Petroleum Society. Publishing services by Elsevier B.V. on behalf of KeAi Communications Co. Ltd. This is an open access article under the CC BY-NC-ND license (http://creativecommons.org/licenses/by-nc-nd/4.0/).

1. Introduction

Hydraulic fracturing is a pivotal technology for the efficient exploitation of unconventional resources such as shale gas and tight oil. The process fundamentally involves the high-pressure injection of proppant-laden fluid into subsurface reservoirs to create and sustain high-conductivity artificial fractures (Kang et al., 2024; Li et al., 2024; Zhao et al., 2024). This process relies on high-pressure pumping units, such as the fracturing pumper shown in Fig. 1, which deliver the slurry through a complex manifold of pipes and elbows to the wellhead. The high-pressure piping system on such equipment contains numerous elbows that are critical points for erosion analysis (Liu et al., 2024a; Peng et al., 2019). Direction-changing components like elbows and tees, while essential for pipeline layout flexibility, have become hot-spots for flow instability and severe erosional wear (Chen et al., 2024; Wang et al., 2016; Yang et al., 2023). As the proppant slurry passes through an elbow, particles with a density significantly greater than the liquid phase deviate from the fluid streamlines due to inertia, leading to high-velocity impingement on the outer wall, followed by rebounds and secondary collisions (Zhou et al., 2020, 2021). This continuous particle-wall impact is the root cause of severe erosion in surface pipelines, wellhead valves, and other critical components. Erosion not only reduces the service life of equipment and incurs substantial maintenance costs but, more critically, can lead to wall thinning and perforation. Such failures risk high-pressure fluid leakage, posing significant operational safety hazards and severely constraining the efficiency and safety of fracturing operations (Li et al., 2019; Xie et al., 2020). Therefore, an in-depth investigation and accurate prediction of the flow dynamics and erosion patterns within elbows are of paramount engineering significance for ensuring the integrity of fracturing equipment and optimizing operational parameters.

* Corresponding author. Research Center of Fluid Machinery Engineering & Technology, Jiangsu University, Zhenjiang 212013, China.
E-mail address: siqiaorui@ujs.edu.cn (Q.-R. Si).
Peer review under the responsibility of Editorial Office of Petroleum Research.

https://doi.org/10.1016/j.ptlrs.2026.01.006
2096-2495/© 2026 Chinese Petroleum Society. Publishing services by Elsevier B.V. on behalf of KeAi Communications Co. Ltd. This is an open access article under the CC BY-NC-ND license (http://creativecommons.org/licenses/by-nc-nd/4.0/).

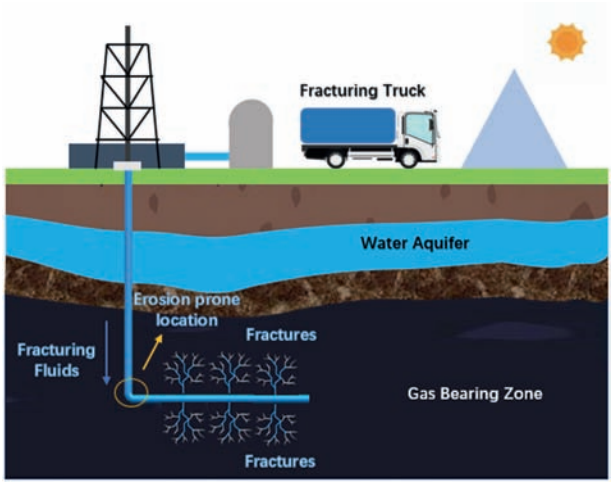


Fig. 1. A typical fracturing pumper unit.

Unlike conventional hydraulic transport, the fracturing fluid used in modern operations is a complex non-Newtonian fluid. Most currently employed systems are water-based fracturing fluids that exhibit pronounced shear-thinning characteristics, meaning their apparent viscosity decreases with an increasing shear rate. This unique rheological property is key to achieving low-friction transport and efficient proppant suspension, however, it also significantly complicates the two-phase flow dynamics within the pipeline. The fluid's rheology directly dictates the drag force, lift force, and turbulent structures acting on the proppant particles, which in turn profoundly influences particle trajectories, velocity distributions, concentration fields, and collision patterns with the pipe wall (Chi et al., 2024). Nevertheless, a majority of current research on fracturing pipeline erosion still relies on simplified Newtonian fluid assumptions or empirical/semi-empirical models (Eppala et al., 2023; Friman Peretz and Levy, 2019; Harbottle et al., 2011; Hashemi et al., 2016; Sun et al., 2015). Although numerous correlations have been developed in recent years to guide practical applications, the lack of a robust theoretical foundation and an in-depth understanding of the complex flow physics remains a critical bottleneck constraining technological advancement. In particular, the flow behavior within elbows is subject to the complex, coupled influence of numerous factors, including material properties, operating conditions, and pipeline geometry (Markauskas et al., 2022; Peng et al., 2023; Zhao et al., 2021). The underlying mechanisms by which shear-thinning rheology governs proppant transport and erosional wear, especially within complex geometries like elbows, remain poorly understood.

Based on the foregoing, it is evident that our comprehension of hydraulic transport phenomena, especially in contexts featuring non-Newtonian fluids and bend-pipe geometries, is not yet complete. This makes the precise theoretical prediction of elbow performance a formidable challenge. As a matter of principle, numerical simulation techniques provide a viable means to supplement the limitations of both theoretical analyses and experimental investigations. The coupled approach combining Computational Fluid Dynamics (CFD) with the Discrete Element Method (DEM) referred to as CFD-DEM has been recognized as a robust tool for addressing these types of problems (Cheng et al., 2017; Hou et al., 2023; Li et al., 2021; Sun et al., 2023; Wan et al., 2023; Wu, 2022). The CFD-DEM methodology enables the direct resolution of the bidirectional coupling between the fluid and discrete particle phases, obviating the need for complex constitutive models for the solid phase stress, and is thus suitable for a wider spectrum of flow conditions (Deng et al., 2024; Liu et al., 2024b; Ma et al., 2022; Sun et al., 2024; Teng et al., 2022; Wang and Ji, 2018). Of particular importance, this method yields detailed information for each particle, including its trajectory, velocity, and impact data (El Geitani and Blais, 2023; Li et al., 2024; Liu et al., 2024c; Wang et al., 2023), which is indispensable for the direct prediction of wall erosion.

However, the majority of existing CFD-DEM studies have primarily focused on scenarios with Newtonian fluids as the carrier medium or have been limited to simple straight-pipe flows. Li et al. (2025) employed the CFD-DEM method to investigate the effects of transport velocity, initial concentration, and particle size grading (PSG). Their results indicated that smaller particles tended to migrate toward the pipe center, while larger particles tended to accumulate near the pipe wall during transport. A more uniform particle distribution was achieved at higher transport velocities and lower initial concentrations. They also found that transport performance, including particle velocity, stability, and energy efficiency, could be enhanced by increasing the proportion of smaller particles (Li et al., 2025). Chen et al. (2015) conducted numerical simulations using a coupled CFD-DEM approach to predict the maximum erosion rates and locations in 90°, 60°, and 45° elbows. Their results showed that while the maximum erosion rates for the three elbows were distinctly different, the location of maximum erosion was consistently identified at or near the elbow outlet (Chen et al., 2015). Schnorr Filho et al. (2022) studied the hydraulic transport of solid particles through a 90° bend under highly confined conditions (pipe-to-particle diameter ratio <5). By tracking particle structures, individual particle motion, and the contact network of the settled bed, they investigated the influence of water flow and particle injection rates on transport rate and settling. A saturated transport rate was found for each water velocity, and for lower velocities, a substantial number of particles settled in the elbow region, forming a persistent, crystal-like lattice over time (Schnorr Filho et al., 2022). Zhao et al. (2022) adopted a combined CFD-DEM method to simulate the erosion process in a 90° elbow with a dilute liquid-solid two-phase flow. The simulations revealed that erosion intensified as the particle mass content increased up to a volume fraction of 10%. Both the pressure gradient force and the virtual mass force were found to reduce erosion along the outer bend, as they pushed particles toward the inner bend and decreased the frequency of particle-wall collisions. Regardless of particle concentration, the particle-turbulence interaction had a lesser effect on coarse particles. For a given particle volume and concentration, sharper particles resulted in less erosion due to reductions in impact angle and particle-wall collisions for the shaped particles (Zhao et al., 2022).

While numerous CFD-DEM studies have investigated proppant transport and erosion in Newtonian fluids, research incorporating non-Newtonian rheology remains comparatively scarce and often overlooks a critical aspect. Existing studies, when they do consider non-Newtonian fluids, have predominantly focused on aspects such as pressure drop or general particle distribution. However, they have largely failed to establish a clear, mechanistic link between the degree of shear-thinning behavior and the resulting erosion patterns, particularly the non-linear and potentially counter-intuitive responses.

This constitutes a significant knowledge gap: it is currently unknown how the competition between fluid-induced particle acceleration (due to reduced viscosity in high-shear zones) and viscous damping (prominent in low-shear zones) quantitatively translates into erosion damage. Consequently, the fundamental question of whether increasing the concentration of shear thinner always reduces erosion has not been answered. Previous studies

have not provided a definitive answer, leaving a critical blind spot in our understanding of erosion in complex fracturing fluids.

To address this specific gap, this study employs a coupled CFD-DEM method, integrated with the Archard wear model, to conduct a systematic numerical investigation. By directly comparing particle transport and erosion in a Newtonian fluid versus shear-thinning fluids of varying concentrations, we aim to be the first to systematically map and explain the non-monotonic erosion response arising from shear-dependent viscosity. The objective is to move beyond general observations and provide a fundamental, mechanism-based understanding of this complex interplay, thereby offering a more nuanced theoretical basis for erosion risk assessment and fracturing fluid design.

While real-world fracturing fluids exhibit complex rheological behaviors, a predominant and critical characteristic of many formulations, such as slickwater and linear gels, is their non-Newtonian, shear-thinning nature. A fundamental understanding of how this specific property influences proppant transport and erosion is essential. Accordingly, this study employs a coupled CFD-DEM method, integrated with the Archard wear model, to systematically investigate solid-liquid two-phase flow in a 90° elbow. By comparing the transport and erosion characteristics of particles in a Newtonian fluid versus shear-thinning fluids (modeled via the power-law relationship), this study aims to: (1) reveal the influence of the fluid's shear-thinning properties on proppant particle trajectories, velocity distributions, and suspension behavior; (2) analyze how different rheological properties alter the internal flow field structure and pressure distribution within the elbow; and (3) quantitatively evaluate and elucidate the impact of fluid rheology on the elbow's erosion rate and the distribution of wear zones. The overarching goal is to deepen the mechanistic understanding of how shear-thinning rheology couples with particle dynamics and erosion phenomena. The insights gained are intended to provide a foundational theoretical basis for assessing erosion risks and informing the principles behind the optimization of more complex fluid systems.

2. Methodology

2.1. Particle motion

According to Newton's second law, the translational and rotational motion of a particle in the DEM model is governed by the following equations:

$$\frac{m_i dv_i}{dt} = \sum_{j=1,j\neq i}^{k} f_{fp,i} + f_{c,ij} + m_i g \tag{1}$$

$$\frac{I_i d\omega_i}{dt} = \sum_{j=1}^{k} T_{ij} \tag{2}$$

Where m_i is the particle mass; v_i is the particle velocity; g is the gravitational acceleration; I_i is the moment of inertia of the particle; ω_i is the particle angular velocity; T_{ij} is the resultant torque acting on particle i from its contact with particle or wall j; $f_{fp,i}$ represents the fluid-particle interaction force; and $f_{c,ij}$ is the contact force exerted on particle i by particle or wall j.

2.2. Fluid flow

The flow of the continuous fluid phase is governed by the volume-averaged continuity and Navier-Stokes equations (Zhou et al., 2021), which can be expressed as:

$$\frac{\partial}{\partial t}\left(\varepsilon_f \rho_f\right) + \nabla\cdot\left(\varepsilon_f \rho_f u_f\right) = 0 \tag{3}$$

$$\frac{\partial}{\partial t}\left(\varepsilon_f \rho_f u_f\right) + \nabla\cdot\left(\varepsilon_f \rho_f u_f u_f\right) = -\varepsilon_f \nabla p + \nabla\left(\varepsilon_f R_f\right) + \varepsilon_f \rho_f g + F_{pf} \tag{4}$$

Where ε_f is the or fluid volume fraction; ρ_f and u_f are the fluid density and velocity, respectively; ∇p represents the fluid pressure gradient; R_f is the fluid stress tensor; and F_{pf} represents the volumetric fluid-particle interaction force, which is calculated as follows:

$$F_{pf} = -\frac{1}{V_{cell}} \sum_{i=1}^{k_c} \left(f_{d,i} + f_{lift,i} + f_{add,i}\right) \tag{5}$$

where k_c is the number of particles and V_{cell} is the volume of a given computational cell; $f_{d,i}$, $f_{lift,i}$, and $f_{add,i}$ are the drag force, lift force, and virtual mass force acting on particle i, respectively.

The fluid stress tensor, R_f, consists of two components, the viscous stress and the Reynolds stress, and is calculated by the following formula:

$$R_f = \eta \nabla u_f + \rho_f \tau \tag{6}$$

where η is the dynamic viscosity of the fluid and τ is the Reynolds stress tensor, expressed as:

$$\tau = \frac{2}{\rho_f}\eta_t S - \frac{2}{3}\frac{\eta}{\rho_f} I, S = \frac{1}{2}\left(\nabla u_f + \left(\nabla u_f\right)^T\right) \tag{7}$$

where η_t is the turbulent viscosity. Based on the study by Zhou et al. (2020), the modulation of turbulence by the particles is considered negligible.

2.3. Fluid-particle interaction

The selection of an appropriate drag model is crucial for enhancing the accuracy of numerical simulations. Accordingly, this study assumes the solid particles to be spherical and employs the Gidaspow drag model (Sinclair, 1995), which is widely applicable to various flow regimes. The model is formulated as follows:

$$\beta = \begin{cases} 150\dfrac{\left(1-\varepsilon_f\right)^2 \mu_f}{\varepsilon_f 2_{d_p}{}^2} + 1.75\dfrac{\left(1-\varepsilon_f\right)\rho_f}{\varepsilon_f d_p}|u-\nu_i|\left(\varepsilon_f < 0.8\right) \\ \dfrac{3}{4}C_D\dfrac{\left(1-\varepsilon_f\right)\rho_f}{d_p}|u-\nu_i|\varepsilon_f{}^{-2.65}\left(\varepsilon_f \geq 0.8\right) \end{cases} \tag{8}$$

where d_p is the particle diameter, and C_D is the drag coefficient, which is calculated as follows:

$$\begin{cases} C_d = \dfrac{24}{Re}\left(1 + 0.15Re^{0.687}\right), Re \leq 1000 \\ C_d = 0.44, Re > 1000 \end{cases} \tag{9}$$

where Re is the particle Reynolds number, given by the formula:

$$Re = \frac{d_p \varepsilon_f \rho_v |u - v_i|}{\mu_f} \tag{10}$$

For the simulation of liquid-solid two-phase flow, the Gidaspow model is one of the most widely used and validated drag

correlations, particularly in commercial CFD software like Fluent. In this study, for non-Newtonian fluid cases, the shear-thinning behavior was accounted for by inputting the locally calculated apparent viscosity into the Gidaspow correlation.

We acknowledge that more recent and specialized drag correlations, developed specifically for power-law fluids (Qi et al., 2018, 2019), can offer higher precision in predicting the particle-fluid interaction force at a micro-scale level. However, the primary objective of this work is to investigate the macro-scale phenomena—specifically, the qualitative trends of elbow erosion and the shift in erosion patterns as a function of fluid rheology.

As our study focuses on a relatively dense slurry flow in a confined geometry (pipe elbow), the particle-particle interactions and the bulk rheological properties of the fluid are expected to play a dominant role in determining the overall particle trajectories and impact dynamics. Previous studies have shown that while different drag models may lead to quantitative differences in parameters like bed expansion or pressure drop, the overarching flow patterns and qualitative trends often remain consistent, especially in systems where inter-particle forces are significant. Therefore, the well-established Gidaspow model, coupled with the local apparent viscosity, is considered a reasonable and effective approach to capture the fundamental physics required for the comparative analysis in this study.

2.4. Non-Newtonian flow model

Fluid rheology is a key factor governing flow characteristics. In this study, four carrier fluids were investigated: pure water and aqueous solutions of carboxymethyl cellulose (CMC) at mass concentrations of 0.2%, 0.3%, and 0.4%. The CMC solutions exhibit shear-thinning (pseudoplastic) behavior, where their apparent viscosity decreases as the shear rate increases. This relationship is described by the Power-law model, expressed as follows:

$$\tau = K\dot{\gamma}^n \tag{11}$$

$$\mu_a = \frac{\tau}{\dot{\gamma}} \tag{12}$$

where τ is the shear stress; $\dot{\gamma}$ is the shear rate; K is the consistency coefficient; n is the flow behavior index; and μ_a is the apparent viscosity.

In this study, the non-Newtonian carrier fluids were described by the power-law constitutive model. It is acknowledged that this model represents a simplification of actual fracturing fluids, which can also exhibit more complex behaviors such as yield stress and thixotropy. However, the power-law model effectively captures the shear-thinning characteristic, which is a dominant feature of many widely used fracturing fluids like slickwater and linear gels. By employing this model, we can isolate and fundamentally analyze the impact of shear-dependent viscosity on proppant dynamics and erosion, without the confounding effects of other rheological parameters. This approach allows for a clearer understanding of the underlying physical mechanisms. The rheological parameters for the aqueous CMC solutions at different mass concentrations, referenced from article published by Pinho and Whitelaw (1990), are listed in Table 1.

Table 1
Rheological properties of CMC aqueous solutions.

TS	$K(pa \cdot s)$	n	$\dot{\gamma}$ range (s^{-1})
0.2%	0.044	0.75	140–12000
0.3%	0.184	0.64	0–12000
0.4%	0.447	0.56	115–12000

2.5. Wear model

The Archard wear model (Archard, 1953), originally proposed by Archard in 1953, is a classic model in tribology for describing adhesive wear. The model establishes a relationship between wear volume, normal contact load, sliding distance, and material hardness, and is widely utilized for wear prediction in fields such as mechanical engineering, materials science, and industrial design. In this study, the Archard wear model is employed to quantify the erosion in the elbow, with its governing equation given as follows:

$$V = k \cdot \frac{F_n s}{H} \tag{13}$$

where V is the wear volume of the wall; k is the dimensionless wear coefficient, which reflects the influence of various factors such as material pairing, surface roughness, lubrication conditions, and temperature on wear; F_n is the normal load (the force acting perpendicular to the contact surface); s is the sliding distance; and H is the material hardness, which in this study is the hardness of the aluminum wall material.

3. Simulation and boundary conditions

3.1. Computational domain and mesh

The three-dimensional computational domain used in this study is depicted in Fig. 2(a). It comprises a 90° pipe elbow with an inner diameter (D) of 24 mm and a curvature radius (R) of 19 mm. To ensure a fully developed flow profile at the elbow's entrance and to minimize any potential backflow effects at the exit, a straight pipe section of 1.2 m (50D) was positioned upstream, and a 1.0 m (42D) section was placed downstream.

The entire domain was discretized using a high-quality structured hexahedral mesh featuring an O-grid topology, as shown in Fig. 2(b). This structure is advantageous for enhancing mesh quality in the near-wall region. A grid independence study was performed to ensure that the simulation results were not dependent on mesh resolution. Three different mesh densities were tested: a coarse mesh (68,648 cells), a medium mesh (110,909 cells), and a fine mesh (200,343 cells). The pressure drop across the elbow for a representative single-phase flow case was used as the key indicator for comparison. As illustrated in Fig. 3, the result from the coarse mesh showed significant deviation, while the discrepancy between the medium and fine meshes was less than 2%. Consequently, to strike an optimal balance between computational accuracy and efficiency, the medium mesh was adopted for all subsequent simulations.

It is important to note that, unlike conventional single-phase flow simulations, near-wall mesh refinement (i.e., inflation layers) was deliberately avoided in this CFD-DEM study. This decision is based on two critical considerations specific to dense particle-laden flows. First, a fundamental requirement in CFD-DEM is that the computational cell size must be significantly larger than the particle diameter (typically >3 dp) to ensure stable and accurate volume fraction and momentum exchange calculations. Aggressive refinement near the wall would violate this principle, leading to numerical instability. Second, in solid-liquid two-phase flow, the constant bombardment of particles against the wall surface continuously disrupts the formation of a stable viscous sublayer. The near-wall physics is dominated by these discrete particle-wall impacts, rendering the primary benefit of a highly refined boundary layer mesh physically irrelevant. Therefore, the chosen meshing strategy is considered

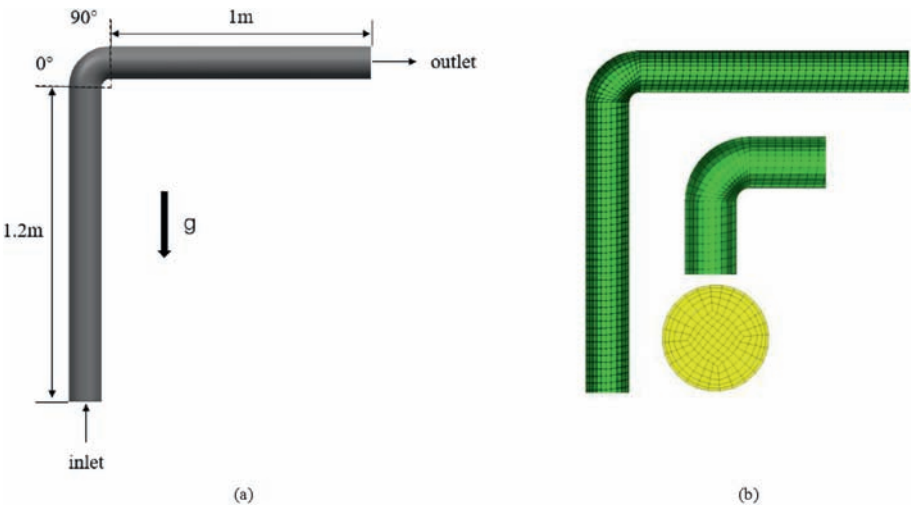


Fig. 2. Computational model setup. (a) Geometric configuration of the 90° elbow, The flow direction is from the bottom inlet to the right outlet. (b) A view of the structured hexahedral mesh used for the fluid domain.

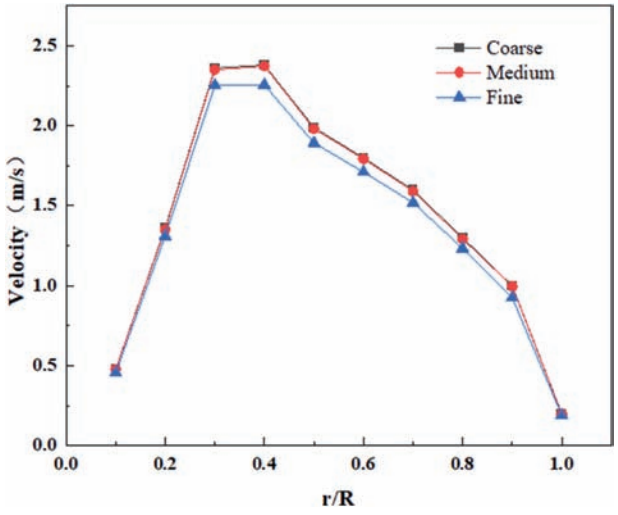


Fig. 3. Grid independence analysis. Comparison of the time-averaged axial velocity profiles at the pipe outlet cross-section for three different mesh resolutions: Coarse, Medium, and Fine.

the most appropriate and physically sound approach for this study.

3.2. Boundary conditions and physical properties

The physical properties of the various CMC carrier fluids and the solid proppant particles used in this study are detailed in Tables 1 and 2. The boundary conditions for the coupled simulation were configured as follows:

Inlet: A velocity-inlet boundary was applied. The carrier fluid entered the domain at a uniform velocity of 1.8 m/s, with a specified turbulence intensity of 5% and a hydraulic diameter of 24 mm. Spherical proppant particles were injected uniformly across the inlet surface at an initial velocity of 1.2 m/s and a constant rate of 17,000 particles per second.

Outlet: A pressure-outlet boundary condition was set with a gauge pressure of zero, allowing particles and fluid to exit the domain freely.

Walls: A no-slip boundary condition was enforced for the fluid phase on all pipe walls. For the discrete phase, particle-wall interactions were governed by DEM contact laws. The coefficients of restitution were set to 0.9, and the coefficient of sliding friction was 0.3.

Table 2
Simulation conditions.

Liquid phase	
Input speed (m/s)	1.8
Temperature (°C)	25
CFD time step (s)	$2.0{\cdot}10^{-4}$
Particles	
Young's modular (pa)	$1.0{\cdot}10^{7}$
Diameter (mm)	1
Density (kg/m^3)	2650
Input speed (m/s)	1.2
Poisson ratio	0.3
Particle-wall sliding friction coefficient	0.3
Particle-particle sliding friction coefficient	0.3
Coefficient of restitution	0.9
Particle flow rate (n/s)	17,000
DEM time step (s)	$2.0{\cdot}10^{-5}$

3.3. Solver configuration and convergence

The transient simulations were performed using the commercial software ANSYS Fluent, with the DEM particle tracking realized through a custom User-Defined Function (UDF) for robust coupling. The standard k-ε model was employed for turbulence modeling. While more advanced models like RSM or DNS can offer higher fidelity (Zheng et al., 2021), their application in industrial-scale, coupled CFD-DEM simulations presents prohibitive computational costs. The standard k-ε model, despite its known limitations in flows with high streamline curvature, has been widely and successfully used in numerous studies on slurry erosion in pipelines and elbows. It provides a robust and computationally efficient framework for capturing the primary flow features and turbulence characteristics that govern particle transport and erosion. Given that the main objective of this study is a comparative analysis of the effects of rheology, the k-ε model is deemed sufficient to provide reliable qualitative trends and engineering-level insights, striking an optimal balance between accuracy and computational feasibility.

The PISO (Pressure-Implicit with Splitting of Operators) algorithm was selected for pressure-velocity coupling, which is well-suited for transient flows. For spatial discretization, a second-order upwind scheme was used for the momentum and turbulence transport equations to ensure high accuracy. The computational time steps were carefully chosen to maintain numerical stability: 2×10^{-4} s for the CFD (fluid) phase and 2×10^{-5} s for the DEM (particle) phase. The simulation for each case was run until the flow reached a hydrodynamically quasi-steady state. This was determined by two criteria: (1) the scaled residuals for all governing equations dropped below a convergence threshold of 10^{-4}, and (2) key physical quantities, such as the pressure drop across the elbow and the particle mass flow rate at the outlet, ceased to show significant fluctuations over time. The influence of gravity was included for both the solid and fluid phases.

4. Results and discussion

4.1. Model validation

The validation of the numerical model was conducted in two steps. First, the fundamental capabilities of the solver were verified against benchmark cases. Second, the applicability of the overall framework for erosion prediction was validated against established findings in the literature.

4.1.1. Fundamental solver verification

In this step, two classical benchmark cases were chosen to verify the solver's ability to handle elementary particle-fluid and particle-particle interactions. Before applying the CFD-DEM model to the complex multiphase flow in the elbow, it is imperative to first verify its capability to accurately capture the most fundamental physics: the interaction between the fluid and a single particle. To this end, we simulated the classic benchmark case of a single particle settling under gravity in a quiescent fluid. In this process, the solid particle reaches a terminal settling velocity when the gravitational force is balanced by the fluid drag forces (including buoyancy). Following the validation methodology of Robinson et al. (2014), the single-particle settling process was simulated. The theoretical terminal velocity for this process can be calculated using Stokes' law.

$$u(t) = \frac{g d_p^2 \left(\rho_p - \rho_f\right)}{18\mu} \left(1 - e^{-\frac{t}{\tau}}\right) \tag{15}$$

where τ is the relaxation time, defined as the time required for the particle to reach its terminal settling velocity from an initial state. It is calculated by the formula:

$$\tau = \frac{\rho_p d_p^2}{18\mu} \tag{16}$$

where $u(t)$ represents the particle's settling velocity. Once steady-state is achieved, the terminal settling velocity u_{term} is given by:

$$u_{term} = \frac{\left(\rho_p - \rho_f\right) g d_p^2}{18\mu_f} \tag{17}$$

For the single-particle sedimentation validation, a rectangular domain of 0.06 m × 0.06 m × 0.16 m was used, with no-slip wall conditions applied to all boundaries (Fig. 4). Gravity was active in the negative z-direction. The simulation involved two fluid phases: air (density = 1 kg/m^3, viscosity = 1×10^{-5} *Pa s*) and water (density = 1000 kg/m^3, viscosity = 0.001 Pa *s*), with the initial water surface at a height of 0.08 m. A single spherical particle with a diameter of 2 mm and a density of 2500 kg/m^3 was placed at a height of 0.1 m, equidistant from the side walls. At the beginning of the simulation ($t = 0$), both the particle and the surrounding fluid were at rest, and the particle was then released.

The simulation was performed using a two-way coupled CFD-DEM model. During the simulation, the particle initially accelerates as it falls through the air, where aerodynamic drag is minimal. Upon penetrating the water surface, the particle experiences a significantly higher drag force, causing its acceleration to decrease. Consequently, the particle's velocity gradually stabilizes, approaching its terminal settling velocity. As shown in Fig. 5, the simulated speed results agree well with the theoretical values. This confirms that the coupled CFD-DEM model accurately captures the particle-fluid interaction forces, thus validating its suitability for the subsequent investigations in this study.

The penetration of a free surface by a particle group serves as another key validation case for the accuracy of the coupled CFD-DEM model. As the denser particles fall into the liquid, they displace the fluid and cause the free surface to rise, a process that fundamentally tests the model's ability to conserve volume in the two-phase particle-fluid system. This validation case follows the methodology of Sun and Sakai (2015). The simulation was performed in the same computational domain as the single-particle test, with a pressure-outlet condition at the top boundary and no-slip conditions on all other walls. The fluid properties for air (density = 1 kg/m^3, viscosity = 1×10^{-5} *Pa s*) and water (density = 1000 kg/m^3, viscosity = 0.001 Pa *s*) were kept consistent. Initially, the water surface was at a height of 0.05 m. A cluster of 4000 spherical particles (diameter = 2 mm, density = 2500 kg/m^3) was positioned at a height of 0.1 m. The particle properties included a Poisson's ratio of 0.3, a Young's modulus of 1×10^7 *Pa*, and particle-particle/particle-wall sliding friction coefficients of 0.3. The cluster was released from rest in the air at $t = 0$ and allowed to settle through the free surface into the water for a total simulation time of 4 s. By $t = 4$ *s*, the particles had settled at the bottom of the domain, and the system reached a new equilibrium. The final water level was measured to be 54.6 mm from the bottom, corresponding to a rise of 4.6 mm (Fig. 6). This simulated rise is in excellent agreement with the theoretical value of 4.652 mm, calculated based on volume displacement. This result confirms the high fidelity of the coupled model in conserving volume during complex multiphase flow simulations.

4.1.2. Framework validation against literature

Addressing the specific application of pipe flow erosion, we further validate our overall modeling framework by referencing established studies in the literature. The combined CFD - DEM and Archard erosion modeling approach has been extensively employed and validated by numerous researchers for predicting erosion in pipe bends and other geometries. For instance, Wu (2022) simulates the flow process of wind-accumulated sand slurry at 1 m/s inlet flow rate with straight pipe bend and uphill by coupled CFD-DEM method. The fluid flow, particle motion and position distribution, pipe erosion and force during the whole process are analyzed based on the selection of a suitable traction model. The results show that the flow velocity of highly viscous slurry at the wall of the pipe is small which can easily lead to the deposition of sand particles, which is proved by the particle velocity cloud diagram. Similarly, Chen et al. (2015) Numerical simulations have been performed by combining CFD code ANSYS FLUENT with DEM code EDEM to predict the maximum erosion rate and location in 90°, 60° and 45° elbows with diameter 40 mm. The fluid is water with inlet velocity 3 m/s, and the particles are 150 μm in diameter and 2650 kg/m^3 in density.

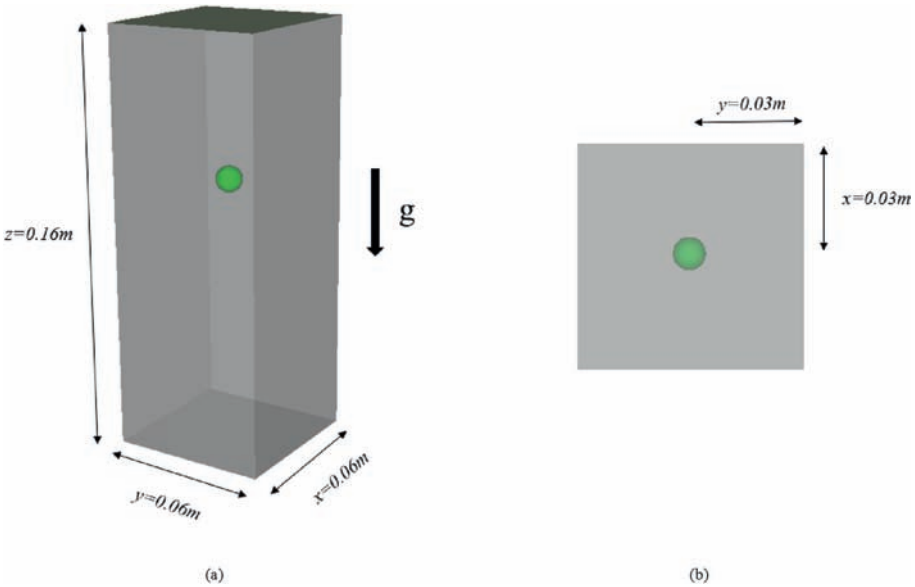


Fig. 4. Geometric model for the single-particle sedimentation validation test. (a) Perspective view with dimensions. (b) Top-down view.

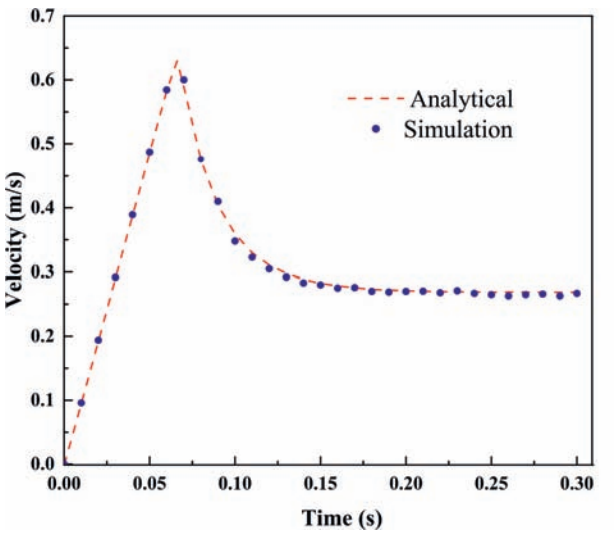


Fig. 5. Validation of the simulated particle settling velocity against the analytical solution.

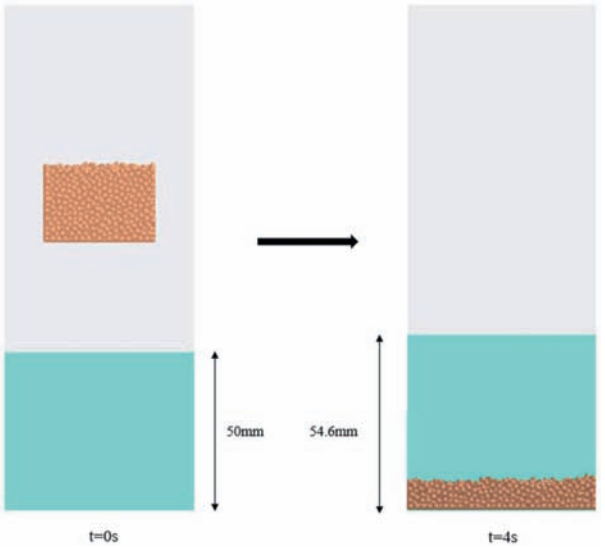


Fig. 6. Validation of the solver's volume conservation for the particle phase. The initial state (t = 0s) and final settled state (t = 4s) are shown.

While the maximum erosion rates of the three are found to be quite different, the maximum erosive locations have been indicated to be at or near the exit of the elbows. In addition, the effect of bend-angle on erosion, particle motion and flow field has been discussed.

Although the exact flow conditions and fluid properties in these studies differ from ours, they collectively demonstrate that the fundamental modeling framework adopted in our work is capable of capturing the key physics of particle-impact erosion in pipe flows. This body of evidence from the literature provides strong support for the applicability and reliability of our chosen methodology for the present investigation.

4.2. Particle flow characteristics

This section investigates the influence of non-Newtonian fluid rheology on the flow characteristics of solid-liquid two-phase transport in pipelines. To this end, a series of simulations were conducted for solid-liquid flows using four different carrier fluids: pure water (a Newtonian fluid) and three aqueous CMC solutions with varying concentrations (non-Newtonian fluids). The physical properties of the carrier fluids and the solid particles are detailed in the preceding tables.

Fig. 7 illustrates the particle flow behavior within the pipe for different carrier fluids, where the particle color represents its velocity. In all simulations, the solid-liquid flow reached a quasi-steady state after 8 s, beyond which no significant changes in flow characteristics were observed. Therefore, the snapshots for analyzing flow patterns, such as the velocity and pressure contours shown, were taken after this time point. As depicted, the particles are initially accelerated by the fluid drag force, as the fluid velocity is higher than the particle velocity. Concurrently, the particles are subjected to gravity, fluid buoyancy, and inter-particle collisions.

Fig. 8 shows the variation of the average particle velocity along the pipe's axial direction. In the vertical upward section, the particle velocity stabilizes as a dynamic equilibrium is established between the upward drag and buoyancy forces and the downward gravitational force. CMC solutions are classic shear-thinning fluids, meaning their apparent viscosity decreases with increasing shear rate. However, even in high-shear regions within the pipe, the effective viscosity of CMC solutions remains substantially higher than that of water. Crucially, higher concentration CMC solutions exhibit a higher zero-shear viscosity, which contributes to a more stable, "plug-like" core flow that enhances the overall particle-carrying capacity. Consequently, with increasing CMC concentration, particles are accelerated more rapidly in the vertical section, and their stable velocity more closely approaches that of the fluid. For the 0.4% CMC solution, the particle velocity in the vertical pipe increased to 1.8 m/s from 1.4 m/s in water, marking a significant enhancement of approximately 28.6%.

As the particle stream enters the elbow, inertia causes the particles to continue their upward trajectory, leading to impacts with the outer wall of the bend. These collisions are energy-dissipating events, resulting in a loss of kinetic energy and a sharp decrease in particle velocity, as indicated by the color shift to blue. The impacts also force the particles to change direction and move horizontally. The higher effective viscosity of the CMC solutions plays a critical role here; it creates a more effective lubrication layer between the particles and the wall and provides better cushioning during collisions, reducing their severity. This also influences the rebound trajectory, preventing particles from clustering tightly along the outer wall. Because the non-Newtonian fluid mitigates the intensity of particle-wall collisions, particles lose less energy in the bend. Subsequently, in the horizontal pipe section, the higher-viscosity CMC solutions more effectively re-accelerate the particles towards the mainstream fluid velocity. This is visualized by the rapid color transition from blue-green at the elbow exit to orange-red downstream, a recovery that becomes more pronounced with increasing CMC concentration.

4.3. Effect of non-Newtonian fluid on particle distribution

Fig. 9 displays the solid volume fraction contours within the pipeline. In the water-based transport, particles in the vertical section exhibit a clear tendency to migrate towards the pipe

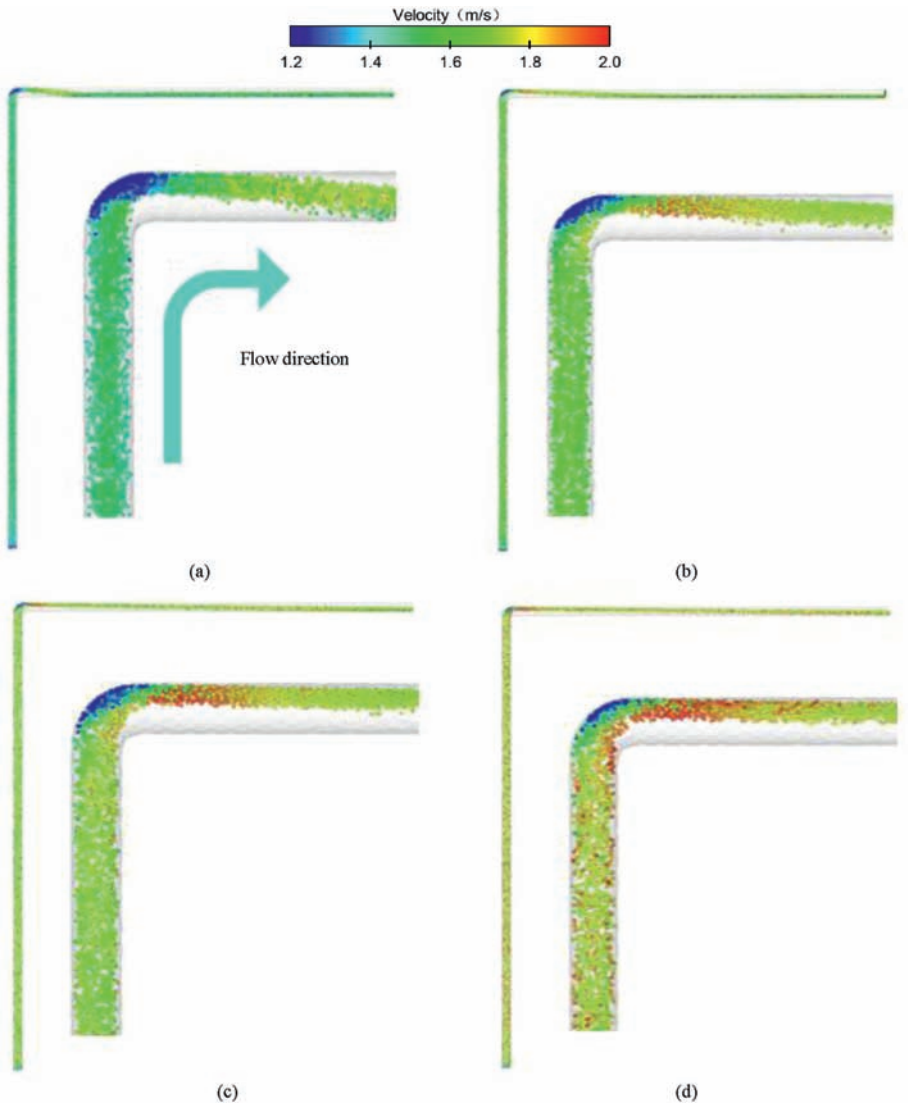


Fig. 7. Instantaneous snapshots of particle distribution, colored by particle velocity magnitude. The snapshots are shown for the four simulated fluid cases after the flow has reached a quasi-steady state: (a) Water, (b) 0.2% CMC, (c) 0.3% CMC, and (d) 0.4% CMC.

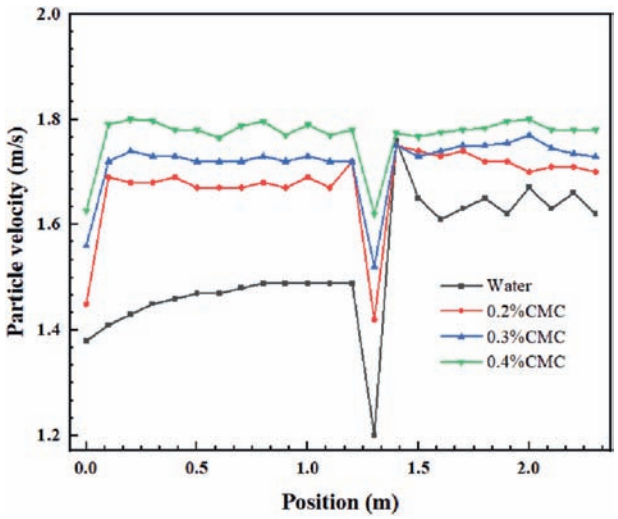


Fig. 8. The snapshots are shown for the four simulated fluid cases after the flow has reached a quasi-steady state: (a) Water, (b) 0.2% CMC, (c) 0.3% CMC, and (d) 0.4% CMC.

centerline, forming a concentrated, relatively continuous particle core. This leaves the near-wall regions with a low particle concentration. This phenomenon is attributed to the Segré-Silberberg effect. In laminar or low-to-moderate Reynolds number turbulent flows, particles are subjected to a combination of a wall-induced lift force pushing them away from the wall and a shear-gradient-induced lift force directing them towards the pipe center. For particles of this size, the equilibrium position established by these forces is typically near the centerline, resulting in the observed core formation.

Conversely, as the CMC concentration increases, the particle distribution across the vertical pipe's cross-section becomes more dispersed, and the central accumulation phenomenon weakens, leading to a more uniform distribution. This observation is consistent with the previously discussed velocity analysis and is more intuitively visualized in the cross-sectional contour at the 45° position of the elbow.

After exiting the elbow, in the horizontal pipe section, particles under the influence of gravity gradually settle and travel along the bottom wall. This is because, in horizontal flow, the fluid's turbulent kinetic energy and lift forces are insufficient to fully counteract the gravitational settling of these denser-than-fluid particles. In stark contrast, particles transported in CMC solutions exhibit a distinctly different suspension behavior. With increasing CMC concentration, they even show a tendency to migrate towards the upper wall. This phenomenon is the result of the combined action of two mechanisms dominated by the shear-thinning properties of the fluid. First, the effective viscosity of the high-concentration CMC solution is much higher than that of water, which not only enhances the axial drag force on the particles but, more importantly, provides strong viscous damping, greatly slowing down the gravitational settling speed of the particles. Second, and more crucially, the shear-thinning property of the fluid leads to the formation of a 'plug flow' velocity profile. Unlike the parabolic profile of Newtonian fluids, the 'plug flow' produces an unusually steep velocity gradient in the near-wall region. According to fluid dynamics principles, this steep shear gradient acting on the settling particles can generate a significantly enhanced, upward-directed hydrodynamic lift force, which effectively counteracts gravity, thereby promoting stable suspension of the particles and even upward migration.

4.4. Effect of non-Newtonian fluid on flow pattern

Fig. 10 presents the fluid velocity contours within the pipeline. A high-velocity core is evident at the pipe's center, while the velocity is low near the wall due to viscous effects. For fully developed flow in a straight pipe, a Newtonian fluid exhibits a parabolic (laminar) or a more blunted (turbulent) velocity profile, with the maximum velocity always at the centerline. The presence of particles disturbs this ideal profile, but the general trend is maintained. This corresponds to the previously discussed Segré-Silberberg effect, where the core-focused particles are accelerated by the high-velocity fluid drag. Compared to water, the fluid velocity profiles for the 0.2% and 0.3% CMC solutions show a less distinct boundary for the high-velocity core; the profile is flatter, with a smaller difference between the peak core velocity and the surrounding fluid. As a shear-thinning fluid, the apparent viscosity of a CMC solution is high in the low-shear central region and low in the high-shear near-wall region, which naturally promotes a flatter, "plug-flow-like" velocity profile. Furthermore, the more dispersed particle distribution in these solutions (as established earlier) leads to momentum exchange over a broader cross-sectional area, causing a "smoothing" of the velocity profile and making the high-velocity core less pronounced. In the 0.4% CMC solution, although the particles are also dispersed, the fluid's significantly higher overall effective viscosity and stronger non-Newtonian character create a more stable and robust plug-flow core. This stable core effectively resists particle-induced disturbances and transports the particles as a whole, which is consistent with its previously observed superior suspension and carrying capacity.

Distinct behaviors are also observed downstream of the elbow. In water, a localized high-velocity zone forms on the inner side of the elbow exit. In contrast, the robust plug-flow nature of the 0.4% CMC solution allows its core flow to maintain integrity through the bend, resulting in a smooth transition without a noticeable localized acceleration zone. In the horizontal section, the contrast becomes even more pronounced. In water, as particles settle due to gravity, they cause a drastic restructuring of the flow field. This settling process obstructs the main flow and dissipates energy. Once a moving bed is formed at the bottom, the upper, particle-lean region allows the fluid to re-develop a high-velocity core in the remaining flow area. Conversely, the exceptional suspension capability of the 0.4% CMC solution prevents particle settling. The fluid and particles move as a more homogeneous-like mixture. The strong plug-flow characteristic is therefore maintained throughout the horizontal pipe, allowing the high-velocity core to persist without the significant flow field restructuring seen in water.

Fig. 11 illustrates the axial pressure drop along the vertical pipe section. As the fluid flows from the inlet to the outlet, the pressure progressively decreases. This is primarily due to the mechanical energy loss required to overcome the viscous frictional resistance at the pipe walls, which manifests as a continuous reduction in static pressure.

Fig. 12 displays the pressure contours at various angular positions within the elbow. A consistent pattern is observed across all cross-sections: the pressure on the outer wall (centrifugal side) is significantly higher than that on the inner wall (centripetal side). This phenomenon arises because the fluid undergoes curvilinear motion in the bend, subjecting it to a centrifugal inertial force. To balance this force and maintain stable turning flow, a radial pressure gradient must be established, directed from the inner to the outer wall, resulting in the observed pressure differential.

Fig. 13 compares the average pressure within the elbow for different carrier fluids, revealing a clear trend: as the CMC

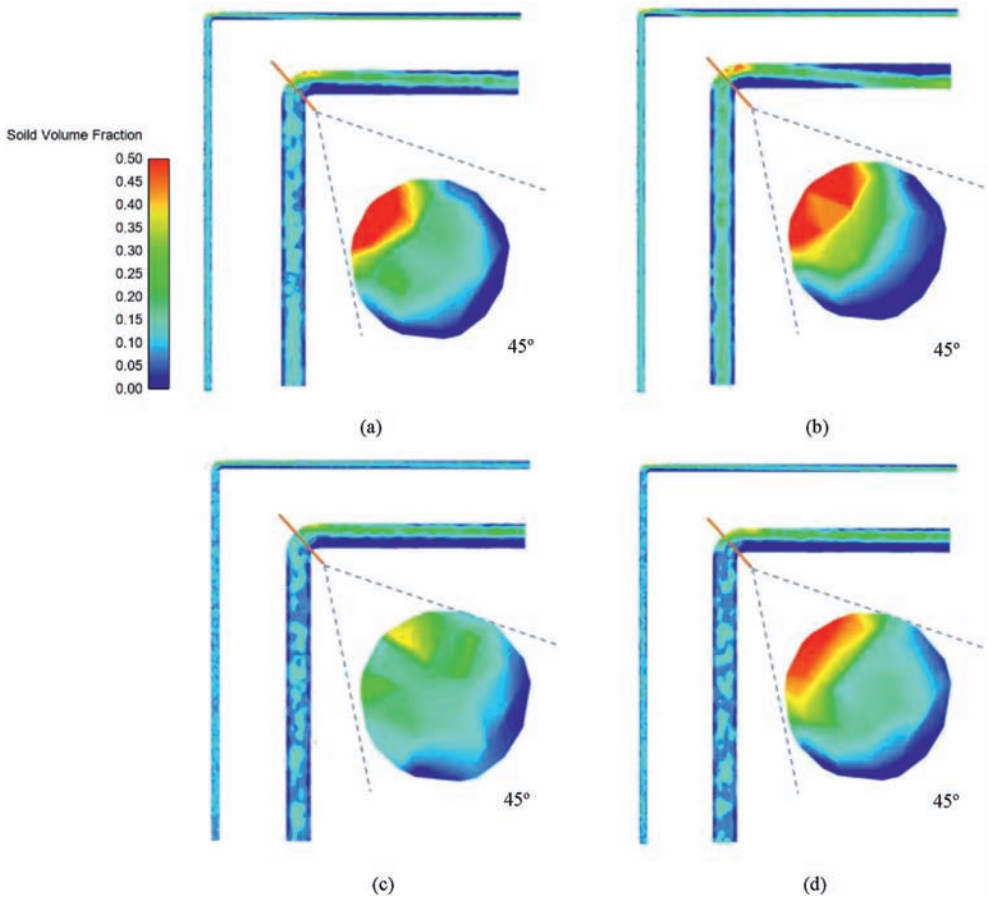


Fig. 9. Contours of solid volume fraction in the elbow. The main view shows the distribution in the central plane. The inset for each case provides a detailed view of the solid volume fraction distribution at the cross-section located 45° into the bend. Cases shown are: (a) Water, (b) 0.2% CMC, (c) 0.3% CMC, and (d) 0.4% CMC.

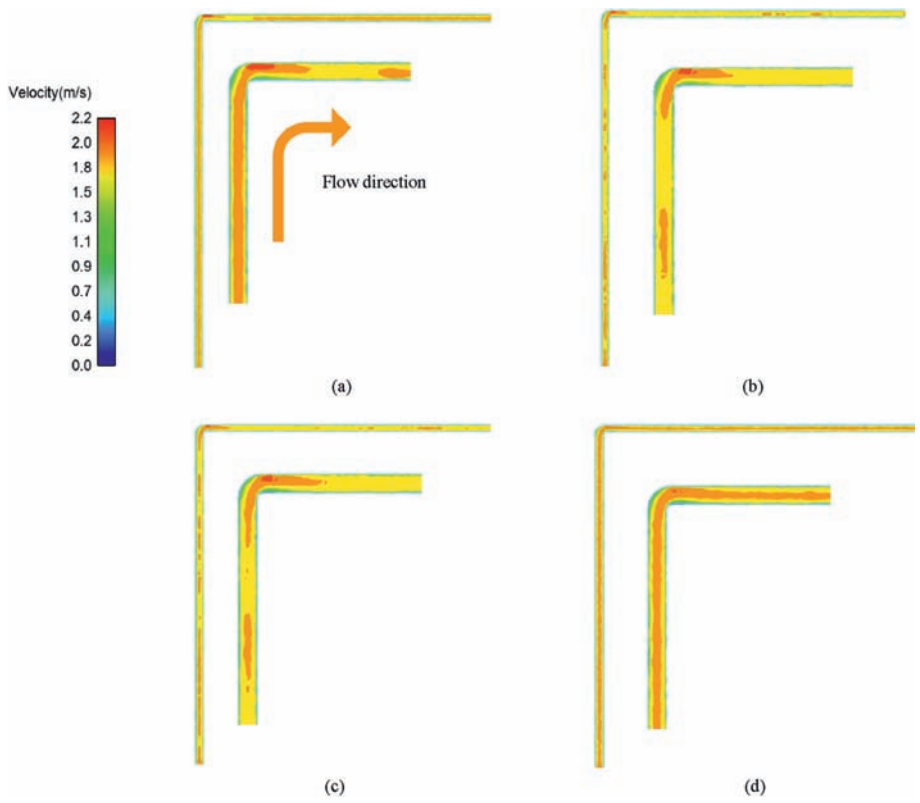


Fig. 10. Contours of fluid velocity magnitude in the central plane for the four different fluid cases: (a) Water, (b) 0.2% CMC, (c) 0.3% CMC, and (d) 0.4% CMC.

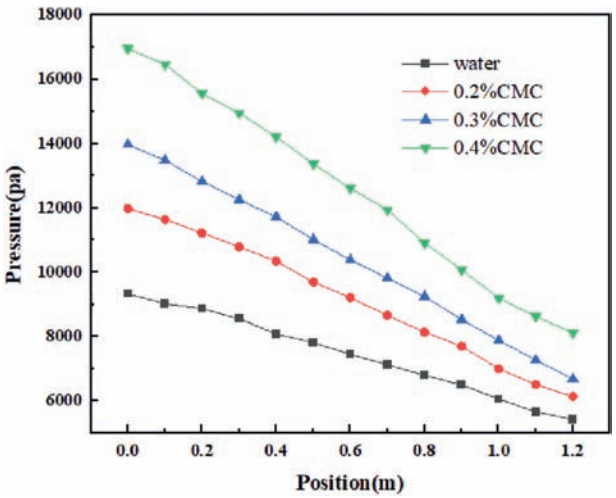


Fig. 11. Pressure distribution along the pipeline for various fluid concentrations.

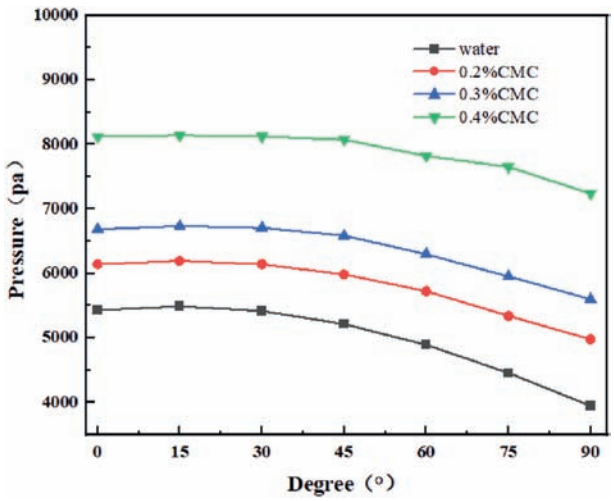


Fig. 13. Angular pressure profiles cross-sectionally averaged in the elbow.

concentration increases (from water to 0.4% CMC), the overall pressure level within the system rises substantially. This is a direct consequence of the rheological properties of the CMC solutions. As non-Newtonian fluids, their viscosity at zero or low shear rates (the zero-shear viscosity) is far greater than that of water, and it increases sharply with concentration. Under the given flow conditions, despite shear-thinning effects, the overall effective viscosity of the CMC solutions remains significantly higher than that of water—a difference that is amplified at higher concentrations. Consequently, maintaining a similar flow state requires overcoming greater flow resistance, leading to a systematic increase in the overall pressure. Specifically, in the elbow section, the pressure for the 0.4% CMC solution reaches approximately 8000 Pa, a substantial increase of about 45.5% compared to the 5500 Pa observed in water.

4.5. Bend erosion

Pipeline erosion is primarily caused by the impact and sliding of solid particles against the pipe wall. Predicting erosion is crucial for estimating the service life of pipelines and identifying critical wear locations, thereby enabling proactive mitigation strategies. In this study, the influence of the non-Newtonian carrier fluid on erosion is analyzed using a coupled CFD-DEM-Wear model, focusing on the erosion depth and erosion rate in the elbow. Fig. 14 presents the erosion depth contours on the elbow after 10 s of flow,

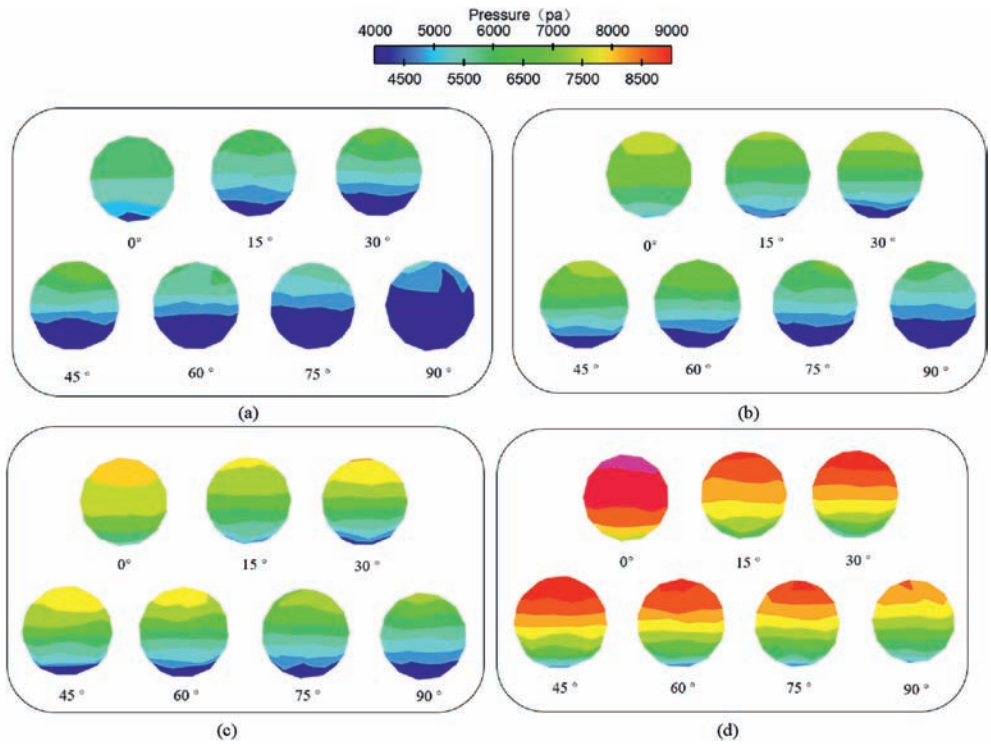


Fig. 12. Cross-sectional pressure distributions in the elbow for different CMC concentrations: (a) Water, (b) 0.2% CMC, (c) 0.3% CMC and (d) 0.4% CMC.

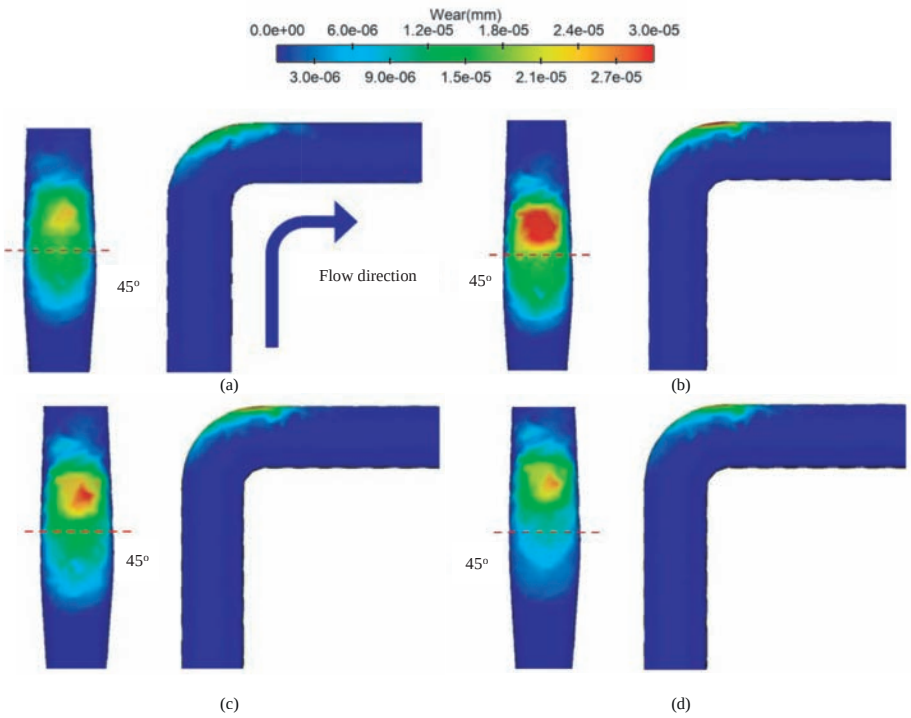


Fig. 14. Cumulative erosion depth on the elbow's inner wall: (a) Water, (b) 0.2% CMC, (c) 0.3% CMC and (d) 0.4% CMC.

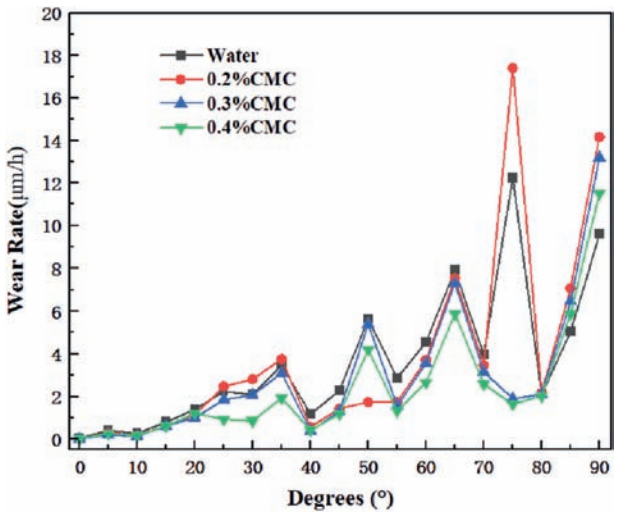


Fig. 15. Wear rate distribution along the elbow's outer wall for various fluids.

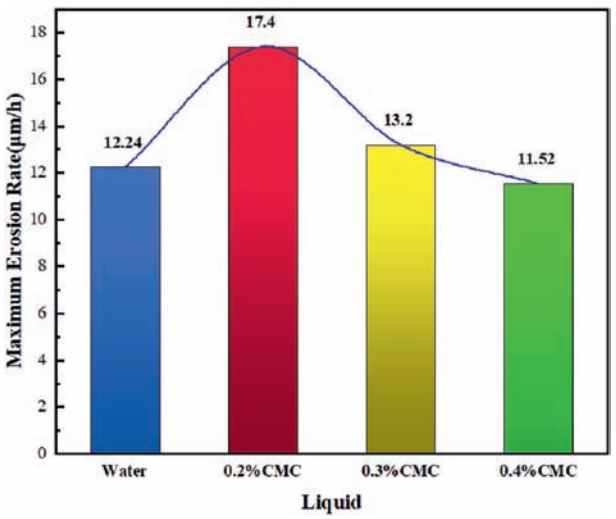


Fig. 16. Comparison of peak erosion rates for different carrier fluids.

a time point chosen to represent the quasi-steady state of the two-phase system. As anticipated from the flow analysis, the maximum erosion zone is located on the outer wall (centrifugal side) of the elbow, near its exit. Notably, as the carrier fluid changes from water to increasingly concentrated CMC solutions, the erosion depth exhibits a noteworthy trend: it first increases with the addition of 0.2% CMC and then gradually decreases as the concentration rises to 0.4%

To quantitatively analyze this behavior, Fig. 15 shows the average erosion rate along the elbow, calculated from the accumulated wear between 10 *s* and 13 *s*. In the initial part of the bend (0–45°), erosion rates are low and comparable across all fluids, as particles have not yet undergone intense, focused impacts with the outer wall. Significant divergence occurs in the middle and latter parts of the bend. For water and the 0.2% CMC solution, the erosion rate is substantially higher, peaking at approximately 77°. In contrast, for higher CMC concentrations, the location of peak erosion is shifted downstream, moving to 90° or even into the subsequent straight pipe section. Furthermore, the magnitude of the peak erosion rate decreases with increasing CMC concentration. This shift occurs because in lower-viscosity fluids like water, inertia causes particles to impact the outer wall earlier and more centrally. In higher-viscosity CMC solutions, the enhanced fluid drag and cushioning effect delay and disperse these impacts, pushing the primary wear zone further downstream. Fig. 16, a bar chart of the maximum erosion rates, quantifies this “increase-then-decrease”

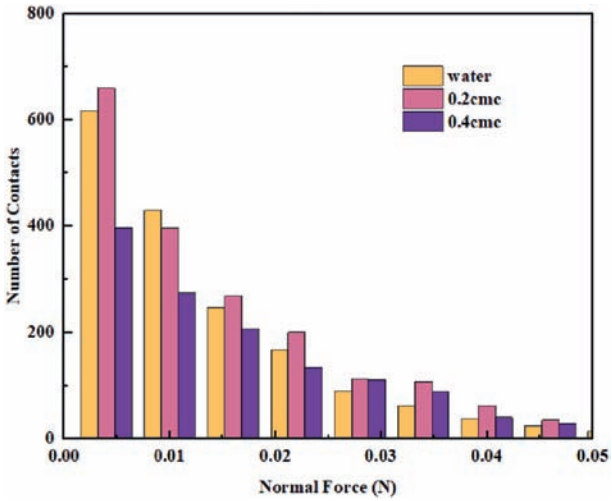


Fig. 17. Distribution of peak normal impact forces on the elbow wall.

relationship. Compared to the water-only case, the peak erosion rate for the 0.2% CMC solution surges by approximately 40%. As the concentration further increases to 0.4%, the erosion rate steadily declines, ultimately falling to a level about 8% below that of pure water.

To provide direct quantitative evidence for the observed erosion behavior, a statistical analysis of the particle-wall normal impact forces was performed. Fig. 17 presents the distribution of peak normal forces for all impact events in the three fluid cases. The figure reveals a clear mechanism for the heightened erosion in the 0.2% CMC solution. Compared to the water case, the 0.2% CMC fluid not only results in a higher total number of impacts but, more importantly, it generates a larger population of impacts across nearly all force ranges, particularly in the medium-to-high force region (>0.01 N). This indicates that the wall is subjected to both more frequent and more intense bombardments. In stark contrast, the 0.4% CMC fluid significantly dampens the impact forces, as evidenced by the consistently lower contact numbers across the entire force spectrum. This force-based statistical evidence robustly supports our conclusion: the enhanced erosion at 0.2% CMC is a direct consequence of an increased number of energetic impacts, while the reduced erosion at 0.4% CMC is due to the fluid's effective force-cushioning effect.

As observed in Figs. 7 and 8, particles in water exhibit pronounced clustering on the outer wall of the elbow, and their velocities decrease sharply upon collision. This concentrated, high-energy bombardment is responsible for the peak erosion observed at approximately 80°. The case of the 0.2% CMC solution reveals a critical, counter-intuitive interplay. Compared to the more concentrated solutions, its viscosity is relatively low, and thus its ability to alter particle trajectories is insufficient to significantly shift the primary impact zone downstream from the location seen in water. However, a crucial combination of factors leads to heightened erosion: 1) particles enter the bend with higher initial velocities than in water (due to better suspension in the vertical pipe), and 2) the fluid's viscosity, while too low to provide effective cushioning, is sufficient to increase the severity of particle-wall interactions compared to the highly inertial impacts in pure water. This combination—higher approach velocity without adequate damping—results in more aggressive and damaging impacts, explaining the sharp increase in the peak erosion rate.

Conversely, as the CMC concentration increases (0.3% and 0.4%), the fluid's effective viscosity became dominant. This provides a superior “carrying” and “cushioning” capacity. Particles are no longer solely driven by inertia to violently strike the outer wall; instead, they are more effectively “guided” and “buffered” by the fluid. Their interaction with the wall transitions from direct, high-angle impacts to more oblique, “glancing” or “sliding” contacts. This mechanism not only reduces the energy of each individual impact but also delays the primary interaction, pushing the main erosion zone towards the elbow exit. Furthermore, the more uniform particle distribution in these highly viscous solutions dissipates the impact forces over a broader area rather than focusing them on a single point. Consequently, the overall erosion rate is significantly lower, and the location of maximum wear is shifted downstream.

Finally, it is pertinent to discuss the context and potential limitations of the current modeling approach. The primary objective of this study was to reveal the overarching trends and physical mechanisms governing erosion in non-Newtonian slurries. For this comparative purpose, the Gidaspow drag model, coupled with local apparent viscosity, was deemed sufficient to capture the dominant, first-order effects. We acknowledge, however, that the use of a drag correlation specifically developed for power-law fluids, such as those proposed by Huang et al. (2024) and Qi et al. (2020), would undoubtedly enhance the quantitative accuracy of the predictions.

We hypothesize that the core findings of this paper—namely, the finding that erosion peaks at an intermediate fluid concentration, and the downstream shift of the erosion hotspot—are robust phenomena driven by the fundamental competition between particle inertia and viscous cushioning. These macro-scale effects are unlikely to be qualitatively altered by refinements in the drag force calculation. A comprehensive study implementing and comparing different advanced drag models via UDF would be a valuable, albeit computationally intensive, direction for future research. This would allow for a precise quantification of the model's sensitivity and further refine the erosion prediction for specific industrial applications.

5. Conclusion

Employing a coupled CFD-DEM approach, this study systematically investigated how fracturing fluid rheology influences proppant transport and elbow erosion. The key findings reveal a complex interplay between fluid properties and erosive wear. A non-monotonic erosion response was identified, where the rate peaked at an intermediate (0.2%) CMC concentration before being suppressed at a higher (0.4%) concentration. This behavior, driven by a competition between reduced viscous drag and enhanced impact cushioning, was accompanied by a downstream shift of the peak erosion hotspot. Scientifically, these results provide the first mechanistic explanation for this counter-intuitive phenomenon driven purely by shear-thinning effects. Industrially, they challenge the conventional assumption that increasing viscosity is always beneficial, suggesting that an optimal ‘sweet spot’ may exist for fluid design to balance proppant transport with equipment longevity.

It is important to acknowledge the limitations of the present study. The use of a power-law model simplifies the complex rheology of real fracturing fluids, which can also exhibit properties such as yield stress and thixotropy. Consequently, the quantitative results and the non-monotonic trends observed should be interpreted as providing insight into the fundamental mechanisms of shear-thinning fluids, rather than as direct predictions for specific field applications. Future research should build upon these

foundational findings. A crucial next step would be to incorporate more sophisticated constitutive models, such as the Herschel-Bulkley or Casson models, to account for yield stress. This would allow for an investigation into how the presence of a yield point alters the "plug-flow" core and particle suspension behavior. Additionally, exploring time-dependent models to capture thixotropic effects would be invaluable for understanding fluid behavior under variable shear conditions experienced during pumping and transport. Such studies will be essential for extending the understanding gained here to a wider and more realistic range of operational conditions and fluid types.

CRediT authorship contribution statement

Chun-Rong Wang: Writing – review & editing, Writing – original draft. **Peng Wang:** Funding acquisition. **Xing-Yang Guo:** Validation. **Shi-Wei Qiao:** Validation. **Jian-Ping Yuan:** Project administration. **Yan-Dong Gu:** Supervision. **Fan Meng:** Visualization. **Qiao-Rui Si:** Project administration.

Declaration of competing interest

The authors declare that they have no known competing financial interests or personal relationships that could have appeared to influence the work reported in this paper.

Acknowledgement

The authors gratefully acknowledge the financial support from the National Natural Science Foundation of China (No. 52106044) and Jiangsu University Senior Talent Start Fund (No. JDG2039).

References

Archard, J.F., 1953. Contact and rubbing of flat surfaces. J. Appl. Phys. 24, 981–988. https://doi.org/10.1063/1.1721448.

Chen, J., Wang, Y., Li, X., He, R., Han, S., Chen, Y., 2015. Erosion prediction of liquid-particle two-phase flow in pipeline elbows via CFD–DEM coupling method. Powder Technol. 275, 182–187. https://doi.org/10.1016/j.powtec.2014.12.057.

Chen, Y., Li, R., Han, W., Zhou, W., 2024. Progressive erosion of 90°elbow wall based on dynamic boundary. Journal of Drainage and Irrigation Machinery Engineering 42, 380–387. https://link.cnki.net/urlid/32.1814.TH.20220907.1708.005.

Cheng, J., Zhang, N., Li, Z., Dou, Y., Cao, Y., 2017. Erosion failure of horizontal pipe reducing wall in power-law fluid containing particles via CFD–DEM coupling method. J. Fail. Anal. Prev. 17, 1067–1080. https://doi.org/10.1007/s11668-017-0340-1.

Chi, M., Zeng, X., Gao, Y., Li, W., Jiang, H., Sun, R., 2024. The erosion rate prediction for the elbow in shale gas gathering and transportation system: RSM and GA-BP-ANN modeling. Powder Technol. 435, 119429. https://doi.org/10.1016/j.powtec.2024.119429.

Deng, L., Lu, H., Yang, J., Sun, P., Hu, Q., Liu, S., 2024. Particle migration and slurry hydraulic resistance in multi-stage reducer pipes. Ocean Eng. 309, 118352. https://doi.org/10.1016/j.oceaneng.2024.118352.

El Geitani, T., Blais, B., 2023. Solid-liquid rotary kilns: an experimental and CFD-DEM study. Powder Technol. 430, 119008. https://doi.org/10.1016/j.powtec.2023.119008.

Eppala, V.C.R., Varghese, M.M., Vakamalla, T.R., 2023. Effect of particle shape on the hydrodynamics of gas-solid fluidized bed. Chem. Eng. Res. Des. 189, 461–473. https://doi.org/10.1016/j.cherd.2022.11.025.

Friman Peretz, M., Levy, A., 2019. Bends pressure drop in hydraulic conveying. Adv. Powder Technol. 30, 1484–1493. https://doi.org/10.1016/j.apt.2019.04.025.

Harbottle, D., Fairweather, M., Biggs, S., 2011. The minimum transport velocity of colloidal silica suspensions. Chem. Eng. Sci. 66, 2309–2316. https://doi.org/10.1016/j.ces.2011.02.012.

Hashemi, S.A., Spelay, R.B., Adane, K.F.K., Sean Sanders, R., 2016. Solids velocity fluctuations in concentrated slurries. Can. J. Chem. Eng. 94, 1059–1065. https://doi.org/10.1002/cjce.22492.

Hou, Y., Song, S., Sun, J., Liu, G., Liu, J., Cui, X., Xu, Q., 2023. Wear regularity of shotcrete conveying Bend based on CFD-DEM simulation. Buildings 13, 415. https://doi.org/10.3390/buildings13020415.

Huang, F., Kuang, S., Ismail, N.I., Zou, R., Yu, A., 2024. Modeling and analysis of particle behavior in fluidized bed bioreactors during Non-Newtonian sewage treatment. J. Water Proc. Eng. 60, 105203. https://doi.org/10.1016/j.jwpe.2024.105203.

Kang, Y., Li, P., Cao, W., Chen, M., You, L., Liu, J., Lai, Z., 2024. Investigation of pore structure alteration and permeability enhancement of shale matrix by supercritical water treatment after hydraulic fracturing. Petroleum 10, 265–274. https://doi.org/10.1016/j.petlm.2022.05.002.

Li, N., Zhu, S., Li, Y., Zhao, J., Long, B., Chen, F., Wang, E., Feng, W., Hu, Y., Wang, S., Jiang, C., 2024. Fracturing-flooding technology for low permeability reservoirs: a review. Petroleum 10, 202–215. https://doi.org/10.1016/j.petlm.2023.11.004.

Li, T., He, L., Shen, J., Yuan, J., Jin, C., Liu, Z., 2025. CFD-DEM modelling of the conveying characteristics of a vertical pipeline for deep-sea mineral particles with wide particle size gradations. Powder Technol. 453, 120654. https://doi.org/10.1016/j.powtec.2025.120654.

Li, Y., Cao, J., Xie, C., 2021. Research on the wear characteristics of a Bend pipe with a bump based on the coupled CFD-DEM. JMSE 9, 672. https://doi.org/10.3390/jmse9060672.

Li, Y., Zhang, H., Lin, Z., He, Z., Xiang, J., Su, X., 2019. Relationship between wear formation and large-particle motion in a pipe bend. R. Soc. Open Sci. 6, 181254. https://doi.org/10.1098/rsos.181254.

Liu, E.-B., Huang, S., Tian, D.-C., Shi, L.-M., Peng, S.-B., Zheng, H., 2024a. Experimental and numerical simulation study on the erosion behavior of the elbow of gathering pipeline in shale gas field. Pet. Sci. 21, 1257–1274. https://doi.org/10.1016/j.petsci.2023.08.034.

Liu, X.-Q., Han, Z.-X., Luo, Z.-L., Lu, H.-L., Sun, Y., You, Q., Guo, T.-K., Qu, Z.-Q., 2024b. Sand control mechanism of radial well filled with phase change material in hydrate reservoir. Pet. Sci. 21, 2571–2582. https://doi.org/10.1016/j.petsci.2024.04.008.

Liu, Y., Xin, C., Tang, J., Xu, S., Yin, Y., 2024c. CFD-DEM simulation and experimental validation of air classification for tobacco particles. Powder Technol. 448, 120318. https://doi.org/10.1016/j.powtec.2024.120318.

Ma, G., Ma, H., Sun, Z., 2022. Simulation of two-phase flow of shotcrete in a bent pipe based on a CFD–DEM coupling model. Appl. Sci. 12, 3530. https://doi.org/10.3390/app12073530.

Markauskas, D., Platzk, S., Kruggel-Emden, H., 2022. Comparative numerical study of pneumatic conveying of flexible elongated particles through a pipe bend by DEM-CFD. Powder Technol. 399, 117170. https://doi.org/10.1016/j.powtec.2022.117170.

Peng, S., Chen, Q., Shan, C., Wang, D., 2019. Numerical analysis of particle erosion in the rectifying plate system during shale gas extraction. Energy Sci. Eng. 7, 1838–1851. https://doi.org/10.1002/ese3.395.

Peng, W., Cao, X., Ma, L., Wang, P., Bian, J., Lin, C., 2023. Sand erosion prediction models for two-phase flow pipe bends and their application in gas-liquid-solid multiphase flow erosion. Powder Technol. 421, 118421. https://doi.org/10.1016/j.powtec.2023.118421.

Pinho, F.T., Whitelaw, J.H., 1990. Flow of non-newtonian fluids in a pipe. J. Non-Newtonian Fluid Mech. 34, 129–144. https://doi.org/10.1016/0377-0257(90)80015-R.

Qi, Z., Kuang, S., Rong, L., Yu, A., 2018. Lattice Boltzmann investigation of the wake effect on the interaction between particle and power-law fluid flow. Powder Technol. 326, 208–221. https://doi.org/10.1016/j.powtec.2017.12.015.

Qi, Z., Kuang, S., Yu, A., 2019. Lattice Boltzmann investigation of Non-Newtonian fluid flow through a packed bed of uniform spheres. Powder Technol. 343, 225–236. https://doi.org/10.1016/j.powtec.2018.11.046.

Qi, Z., Kuang, S.B., Qiu, T.S., Yu, A.B., 2020. Lattice Boltzmann investigation on fluid flows through packed beds: interaction between fluid rheology and bed properties. Powder Technol. 369, 248–260. https://doi.org/10.1016/j.powtec.2020.05.046.

Robinson, M., Ramaioli, M., Luding, S., 2014. Fluid–particle flow simulations using two-way-coupled mesoscale SPH–DEM and validation. Int. J. Multiphas. Flow 59, 121–134. https://doi.org/10.1016/j.ijmultiphaseflow.2013.11.003.

Schnorr Filho, E.A., Lima, N.C., Franklin, E.M., 2022. Resolved CFD-DEM simulations of the hydraulic conveying of coarse grains through a very-narrow elbow. Powder Technol. 395, 811–821. https://doi.org/10.1016/j.powtec.2021.10.022.

Sinclair, J.L., 1995. Multiphase flow and fluidization: Continuum and kinetic theory descriptions. Powder Technol. 83, 287. https://doi.org/10.1016/0032-5910(95)90055-1.

Sun, B., Fan, J., Wen, D., Chen, Y., 2015. An experimental study of slurry erosion involving tensile stress for pressure pipe manifold. Tribol. Int. 82, 280–286. https://doi.org/10.1016/j.triboint.2014.07.025.

Sun, C., Xu, Z., Xiao, Y., Cui, G., Xiao, Z., Cui, W., Wang, P., Jia, L., 2024. Study of hydraulic transport characteristics and erosion wear of twisted four-lobed pipe based on CFD-DEM. Particuology 95, 356–369. https://doi.org/10.1016/j.partic.2024.10.011.

Sun, X., Sakai, M., 2015. Three-dimensional simulation of gas–solid–liquid flows using the DEM–VOF method. Chem. Eng. Sci. 134, 531–548. https://doi.org/10.1016/j.ces.2015.05.059.

Sun, Z., Chen, L., Gao, K., Ma, G., Ma, H., Li, P., Zhang, Y., 2023. Additional pressure loss coefficient of pneumatic conveying of moist-mixed materials for shotcrete based on CFD-DEM method. J. Build. Eng. 76, 107242. https://doi.org/10.1016/j.jobe.2023.107242.

Teng, S., Kang, C., Ding, K., Li, C., Zhang, S., 2022. CFD-DEM simulation of the transport of manganese nodules in a vertical pipe. Appl. Sci. 12, 4383. https://doi.org/10.3390/app12094383.

Wan, Z., Yang, S., Tang, D., Yuan, H., Hu, J., Wang, H., 2023. CFD-DEM investigation of gas–solid swirling flow in an industrial-scale annular pipe. Chem. Eng. J. 461, 141975. https://doi.org/10.1016/j.cej.2023.141975.

Wang, Q., Zhang, L., Hu, J., Wang, H., Li, K., 2016. A dynamic and non-linear risk

evaluation methodology for high-pressure manifold in shale gas fracturing. J. Nat. Gas Sci. Eng. 29, 7–14. https://doi.org/10.1016/j.jngse.2015.12.049.
Wang, S., Ji, S., 2018. Coupled DEM–FEM analysis of ice-induced vibrations of a conical jacket platform based on the domain decomposition method. IJOPE 28, 190–199. https://doi.org/10.17736/ijope.2018.ik03.
Wang, S., Liang, D., Ji, S., 2023. DEM study on mixing behaviors of concave-shaped particles in rotating drum based on level-set method. Powder Technol. 430, 118961. https://doi.org/10.1016/j.powtec.2023.118961.
Wu, B., 2022. CFD-DEM based wind-deposited sand high concentration slurry pipe transport characteristics and erosion study. J. Phys., Conf. Ser. 2280, 012041. https://doi.org/10.1088/1742-6596/2280/1/012041.
Xie, D., Wu, Y., Zhang, Z., Wang, T., Chen, P., Cui, Y., Li, C., Feng, S., 2020. Numerical simulation of elbow erosion in liquid-solid two-phase flow. IOP Conf. Ser. Mater. Sci. Eng. 740, 012169. https://doi.org/10.1088/1757-899X/740/1/012169.
Yang, Siqi, Fan, J., Zhao, S., Dai, S., Han, L., Wang, J., Yang, Shangyu, Zhang, L., Li, J., 2023. Experimental study on erosion behavior of fracturing pipelines involving fluctuating stress. Wear 518–519. https://doi.org/10.1016/j.wear.2023.204626, 204626.
Zhao, J., Wu, T., Pu, W., Daijun, D., Chen, Q., Chen, B., Li, J., Huang, Y., 2024. Application status and research progress of CO2 fracturing fluid in petroleum engineering: a brief review. Petroleum 10, 1–10. https://doi.org/10.1016/j.petlm.2023.12.001.
Zhao, R., Zhao, Y., Si, Q., Gao, X., 2022. Effects of different characteristics of the dilute liquid-solid flow on the erosion in a 90° bend. Powder Technol. 398, 117043. https://doi.org/10.1016/j.powtec.2021.117043.
Zhao, Y., Yan, Y., Zhou, X., Yao, J., Wang, C.-H., 2021. Numerical investigation of electrostatic effect on particle behavior in a 90 degrees bend. Adv. Powder Technol. 32, 810–824. https://doi.org/10.1016/j.apt.2021.01.022.
Zheng, E., Rudman, M., Kuang, S., Chryss, A., 2021. Turbulent coarse-particle Non-Newtonian suspension flow in a pipe. Int. J. Multiphas. Flow 142, 103698. https://doi.org/10.1016/j.ijmultiphaseflow.2021.103698.
Zhou, M., Kuang, S., Luo, K., Zou, R., Wang, S., Yu, A., 2020. Modeling and analysis of flow regimes in hydraulic conveying of coarse particles. Powder Technol. 373, 543–554. https://doi.org/10.1016/j.powtec.2020.06.085.
Zhou, M., Kuang, S., Xiao, F., Luo, K., Yu, A., 2021. CFD-DEM analysis of hydraulic conveying bends: interaction between pipe orientation and flow regime. Powder Technol. 392, 619–631. https://doi.org/10.1016/j.powtec.2021.07.052.
Li, H., Zhu, X., Wang, Z., Liu, Y., 2024. Numerical simulation of gas-solid flow characteristics in pressurized bubbling fluidized bed based on CFD-DEM method. J. Drain. Irrigation Mach. Eng. 42, 570–575.